Scintillation time dependence and pulse shape discrimination in liquid argon

W. H. Lippincott,[1] K. J. Coakley,[2] D. Gastler,[3] A. Hime,[4] E. Kearns,[3] D. N. McKinsey,[1,*] J. A. Nikkel,[1] and L. C. Stonehill[4]

[1]*Department of Physics, Yale University, New Haven, Connecticut 06511, USA*

[2]*National Institute of Standards and Technology, Boulder, Colorado 80305, USA*

[3]*Department of Physics, Boston University, Boston, Massachusetts 02215, USA*

[4]*Los Alamos National Laboratory, Los Alamos, New Mexico 87545, USA*

(Received 10 January 2008; revised manuscript received 28 June 2008; published 2 September 2008)

Using a single-phase liquid argon detector with a signal yield of 4.85 photoelectrons per keV of electronic-equivalent recoil energy (keVee), we measure the scintillation time dependence of both electronic and nuclear recoils in liquid argon down to 5 keVee. We develop two methods of pulse shape discrimination to distinguish between electronic and nuclear recoils. Using one of these methods, we measure a background- and statistics-limited level of electronic recoil contamination to be 7.6×10^{-7} between 52 and 110 keV of nuclear recoil energy (keVr) for a nuclear recoil acceptance of 50% with no nuclear recoil-like events above 62 keVr. Finally, we develop a maximum likelihood method of pulse shape discrimination based on the measured scintillation time dependence.

DOI: 10.1103/PhysRevC.78.035801 PACS number(s): 29.40.Mc, 61.25.Bi, 95.35.+d

I. INTRODUCTION

Recent years have seen an increase in the number of experiments using noble liquids as materials for detecting weakly interacting massive particles (WIMPs), a well-motivated dark matter candidate [1]. The current best limit for the spin-independent WIMP-nucleon cross section for a 60-GeV WIMP mass is 4.6×10^{-44} cm^2, set by the Cryogenic Dark Matter Search (CDMS) experiment [2]. Because many noble liquids have high scintillation yields, are easily purified of radioactive impurities, and are likely to be scalable to large masses with relative ease, they hold great promise for this application. The current best limit from a noble liquid detector is 8.8×10^{-44} cm^2 at 100 GeV, set by XENON10 [3]. Noble liquid detectors with larger target masses will likely improve on these limits.

The key to the noble liquid dark matter detectors is discriminating between nuclear recoil events that constitute a WIMP signal and electronic recoil events that form the primary backgrounds. The XENON and ZEPLIN experiments are designed to collect both scintillation light and ionization from liquid xenon [4,5]. These are dual-phase detectors that use both scintillation light and ionization charge collection to discriminate between event classes, as nuclear recoils and electronic recoils produce different ratios of charge to light. Liquid argon is an attractive alternative to liquid xenon because of the lower cost of natural argon and its simpler purification requirements. The WIMP Argon Programme (WARP) and Argon Dark Matter (ArDM) experiments employ dual-phase detectors that use liquid argon as the target [6,7].

Alternatively, a single-phase detector collecting solely scintillation light might distinguish between electronic and nuclear recoils using pulse shape discrimination (PSD). In 1978, Kubota *et al.* showed that the time dependence of scintillation light in liquid xenon and liquid argon is significantly different for heavy ionizers such as α particles and fission fragments than for light ionizers such as β decay and Compton-scattered electrons [8]. This is because scintillation in liquid noble gases is produced by the decay of excimers that can exist in either singlet or triplet molecular states, which have very different lifetimes (Table I). The slow scintillation light emitted by triplet molecules can be suppressed in intensity by destructive triplet interactions, primarily Penning ionization and electron-triplet spin exchange; it is believed that these reactions are stronger for high excitation densities such as those produced by nuclear recoils, causing the observed time dependences. Therefore, the relative amplitudes of the fast and slow components can be used to determine which type of excitation occurred for a given event.

Pulse shape discrimination based on the timing of scintillation light has been studied for use with several noble liquids. In liquid helium, PSD has been studied to separate electronic recoil events from ^{3}He$(n,p)^3$H events in the search for the permanent electric dipole moment of the neutron [11]. PSD has also been used to suppress γ-ray backgrounds in liquid xenon [12,13]. McKinsey and Coakley [14] pointed out that the much longer triplet lifetime in liquid neon should allow superior PSD, which has recently been verified experimentally [10]. Following this observation, Boulay and Hime recognized that the similar properties of liquid argon could in principle achieve PSD with part per billion levels of electronic recoil contamination (ERC) [15]. ERC is defined to be the probability of incorrectly classifying an electronic recoil event as a nuclear recoil event given a particular level of nuclear recoil acceptance. An ERC of 10^{-8} or better is required to perform a competitive WIMP search using liquid argon because of the presence of the radioactive isotope ^{39}Ar, which produces about 1 Bq per kg of atmospheric argon [16–18]. The WARP collaboration has used scintillation timing in combination with an ionization signal to reduce electronic recoil backgrounds in liquid argon [19]. The Dark Matter Experiment using Argon Pulse Shape Discrimination (DEAP)

*daniel.mckinsey@yale.edu

TABLE I. Lifetimes of the singlet and triplet states for neon, argon, and xenon excimers [9,10].

	Singlet lifetime (ns)	Triplet lifetime (ns)
Ne	$<18.2 \pm 0.2$	14900 ± 300
Ar	7.0 ± 1.0	1600 ± 100
Xe	4.3 ± 0.6	22.0 ± 2.0

has demonstrated a background limited ERC of 5×10^{-6} using the DEAP-0 single-phase detector for nuclear recoil energies above 1 MeV [20]. At a given energy, ERC improves exponentially with scintillation light collection efficiency. For this reason, efficient scintillation light detection is the primary requirement for performing a sensitive WIMP search with negligible background at a suitably low energy threshold.

In this paper we describe measurements of scintillation in liquid argon due to low-energy nuclear and electronic recoils in the energy range relevant to a WIMP dark matter search. We measure the scintillation time dependence of liquid argon for both event classes. We develop two basic PSD methods and measure the level of discrimination in our apparatus. Finally, we use the measured time dependence to develop a maximum likelihood method of PSD.

II. EXPERIMENTAL DETAILS

A. Detector design

The apparatus consists of a 3.14-liter active volume of liquid argon viewed by two 200-mm-diameter photomultiplier tubes (PMTs) [21], all contained within a stainless steel vessel and vacuum Dewar. Figure 1 shows a schematic of the central volume and PMTs. The active region is defined by a Teflon cylinder 200 mm in diameter and 100 mm high with two 3-mm-thick fused-silica windows enclosing the top and bottom. The PMTs are held in place by Teflon rings above and below the central volume and view the active region through the windows. They are powered by positive high voltage with a typical gain of approximately 4×10^7.

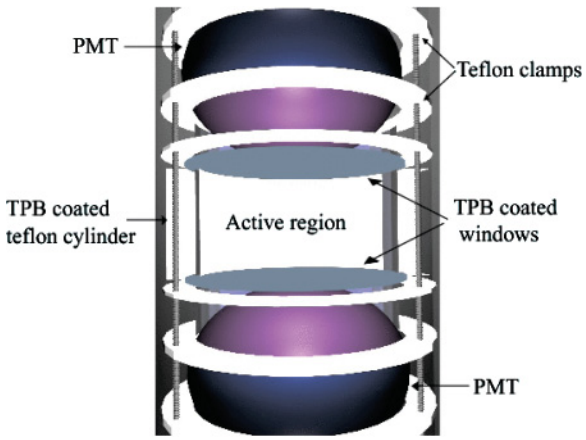

FIG. 1. (Color online) Schematic representation of the scintillation cell.

Because liquid argon scintillates in the ultraviolet ($\approx$128 nm) [22], all inner surfaces of the Teflon and windows are coated with a thin film of tetraphenyl butadiene (TPB) [23] by use of a Tectra Mini-Coater evaporation system [24].[1] The TPB shifts the wavelength of the ultraviolet light to approximately 440 nm so that it can pass through the windows and be detected by the PMTs. Both windows are coated with (0.20 ± 0.01) mg/cm^2 of TPB, while the Teflon cylinder is coated with (0.30 ± 0.01) mg/cm^2. The Teflon cylinder, windows, and PMTs are all immersed directly in liquid argon and contained within a 25-cm-diameter by 91-cm-tall stainless steel vessel.

The stainless steel vessel is, in turn, housed inside a vacuum Dewar, and argon gas is introduced into the system through a tube on top of the Dewar. The argon is liquefied in a copper cell mounted to the end of a pulse-tube refrigerator [25] inside the Dewar before flowing through a tube to the stainless steel vessel. All components that come into contact with the gas or liquid are baked to at least 60°C, and the ultra-high-purity argon gas (99.999%) is passed through a heated gas-purification getter [26] before entering the vessel. In addition, the argon is continually circulated through the getter and reliquefied at a rate of at least 2.0 standard liters per minute (slpm) to ensure that high purity is maintained. The stability of the system is discussed further in Sec. II C.

The data acquisition (DAQ) system is custom-built around VME-bus waveform digitizers (WFDs); a sample WFD trace from a scintillation event in argon can be seen in Fig. 2. The PMT signals from the detector are divided three ways by a linear fan out with two copies of the signal sent to the WFDs and one sent to a triggering system. Each WFD has four channels that record eight-bit samples at 500 MHz. These samples are stored in a separate programmable-length memory buffer for each channel. For all data presented here, the record length is set to 26 μs. The two copies of the PMT

[1]Commercial equipment, instruments, or materials are identified in this paper in order to adequately specify the experimental procedure. Such identification implies no recommendation or endorsement by NIST, nor does it imply that the materials or equipment identified are necessarily the best available for the purpose.

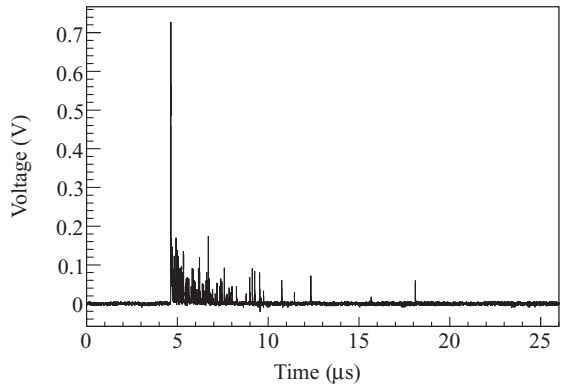

FIG. 2. Example of an electronic recoil event from a single PMT, digitized by the eight-bit WFD, sampling at 500 MHz. Four μs of presamples are recorded to measure the baseline.

waveforms are recorded separately at unity gain and at an attenuation of ten to increase the effective dynamic range of the eight-bit digitization. The buffer is continually filled but saved to disk only when the triggering system registers a fraction of a photoelectron in both PMTs within a 100-ns coincidence window. Once a trigger has been registered, the DAQ records the event for 22 μs, leaving an additional 4 μs of baseline presamples in the data (see Fig. 2). The data are read to a computer via fiber-optic cable, and after the computer has recorded all 26 μs of data, it resets the system for the next event. The data collected by the DAQ software are saved in a ROOT-based file structure [27].

B. Data collection

All data collected are processed in software. First, for each PMT, the two gain scales are combined into a single waveform. Three μs of baseline presamples are averaged to obtain a baseline and baseline root-mean-square. The baseline is then subtracted from the trace. Ideally, we would count single photoelectrons in a pulse, but since we detect many photoelectrons that produce signals overlapping in time, we integrate the trace to determine the total number of photoelectrons. To mitigate the integration noise, we restrict the range of the integral to 50-ns regions in which the trace voltage crosses a threshold of four times the baseline root-mean-square (a threshold of approximately 2/5 the height of a photoelectron). This method is a hybrid of single photoelectron counting and pulse integration.

We then apply three cuts to all data. One cut removes events in which either PMT saturates due to excessive light exposure by rejecting events above an experimentally determined threshold of approximately 2000 times the single photoelectron pulse area. A second cut removes events for which the trigger time (defined as the time at which the voltage rises above 20% of its maximum value) differs by greater than 20 ns between the two PMTs. The third cut is designed to eliminate events that produce light in the windows or the glass of the PMTs. An asymmetry parameter A is defined as

$$A = \frac{S_T - S_B}{S_T + S_B}, \tag{1}$$

where S_T and S_B are the signal areas in the top and bottom PMTs. For most data, we require $-0.275 < A < 0.375$, due to a slightly larger gain in the top PMT. This cut is relaxed to $|A| < 0.4$ to improve the statistics of the nuclear recoil data described below.

We use a 10-μCi ^{22}Na source to produce electronic recoils. In 90% of ^{22}Na decays, a positron is emitted that immediately annihilates in the surrounding materials to produce 511-keV γ rays with equal and opposite momenta, or "back-to-back." We use the second γ ray to electronic recoil events in the liquid by triggering on a coincidence within a 100-ns window between the PMTs in the argon and a NaI crystal scintillator placed back-to-back with our apparatus. This event tagging reduces backgrounds in our data from other radioactive decays and cosmic rays. To further decrease neutron backgrounds, we place one layer of water-filled containers above and around the sides of the Dewar. These containers are cubes of side 30 cm in length and hold 20 liters of water.

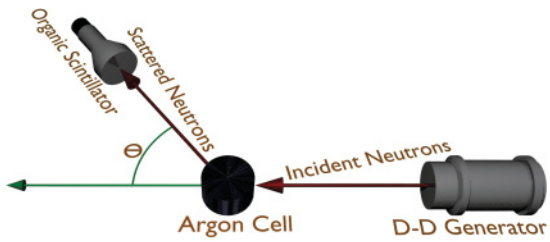

FIG. 3. (Color online) Schematic of the neutron scattering setup.

In addition to the three universal cuts, we apply two additional cuts to ensure data purity. In software we narrow the coincidence window between the liquid argon PMTs and the NaI crystal to 30 ns. We also make an energy cut to the NaI energy spectrum to select 511-keV events in the NaI crystal. In the liquid argon, the majority of the 511-keV γ Compton scatter, producing events with a continuum of deposited energies.

To investigate the detector response to nuclear recoils, we use a portable deuterium-deuterium neutron generator [28] as a source of 2.8-MeV neutrons and a PMT viewing BC501A organic scintillator as a secondary detector. Both the generator and the organic scintillator are placed approximately 1.63 m from the center of the active volume. We require a detection of a scintillation event in the liquid argon, followed within 200 ns by an event in the organic scintillator. The experimental setup can be seen schematically in Fig. 3. By changing the scattering angle θ, we can choose the energy of the nuclear recoils observed in the liquid, $E_{\rm rec}$, using simple kinematics:

$$E_{\rm rec} = \frac{2E_{\rm in}}{(1+M)^2}[1 + M - \cos^2(\theta) - \cos(\theta)\sqrt{M^2 + \cos^2(\theta) - 1}], \tag{2}$$

where $E_{\rm in}$ is the incident neutron energy and M is the atomic mass of the target.

Since we know the energy of the neutron, we can calculate the time-of-flight of a neutron that scatters in the liquid argon and the organic scintillator. We then apply a time-of-flight cut between the liquid argon cell and the organic scintillator to distinguish between γ rays and neutrons, as the neutron generator produces both. In general, the time-of-flight cut requires an event to occur in the organic scintillator 60–90 ns after the event in the liquid argon. In addition, we make a PSD cut in the organic scintillator data to further eliminate electronic recoils.

We also collect background data by looking at events in the liquid argon with no external source present. These background data provide an estimate of the accidental background rate that may be contaminating the γ-ray data sets, which will be discussed further in Sec. III B.

C. Detector calibration

We use a 10-μCi sealed ^{57}Co source for daily calibrations. This source produces 122-, 137-, and 14.4-keV γ rays, with

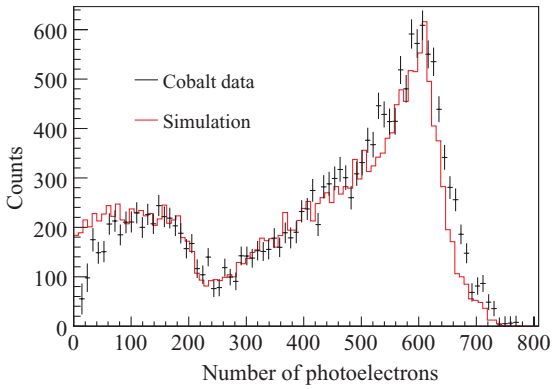

FIG. 4. (Color online) Example spectrum of ^{57}Co data, along with a simulation done using the Reactor Analysis Tool [30].

branching ratios of 86%, 11%, and 9%, respectively. Any scintillation event in liquid argon produces a significant triplet component; since this component is spread out over many μs, it appears in the signal as many single photoelectrons well separated in time (for example, a number of single photoelectrons appear after 7 μs in Fig. 2). Therefore, we measure the gain of the PMTs using the ^{57}Co source by selecting single photoelectrons from the tail end of each pulse. The PMT traces are divided into 75-ns regions centered on times at which the trace crossed an experimentally determined threshold of roughly 1/3 of a photoelectron. These regions are then integrated to obtain the single photoelectron pulse area. The typical gain for the PMTs is approximately 4×10^7.

Figure 4 shows an example ^{57}Co spectrum along with a simulation done with the Reactor Analysis Tool, a toolkit of GEANT4 developed by the Braidwood Collaboration [29,30]. From the simulation, we find that the position of the primary peak is dominated by the 122-keV γ photoabsorption process. The simulation parameters describing absorption and reflection of the materials in the detector are tuned to match the observed signal yield, and the spectral shapes line up nicely.

By comparing the integrated signal corresponding to the 122-keV peak to that of a single photoelectron, we measure the signal yield of the detector to be 4.85 photoelectrons per keV electron equivalent (keVee), where keVee refers to the amount of energy deposited by an electronic recoil. The response of the detector was stable to within 5% during the four months of data acquisition.

We use the 122-keV ^{57}Co peak to provide a daily energy calibration. To check the quality of that calibration, we use the 511-keV γ rays produced by the ^{22}Na source as a second point of reference. When calibrated using the ^{57}Co source and the assumption that the signal scales linearly with deposited energy, the 511-keV absorption line appears in the ^{22}Na spectrum as expected to within 1%. In addition, simulations of 511-keV γ rays are consistent with the data.

Impurities in the detector can build up over time via outgassing. These impurities can quench argon excimers or absorb emitted UV photons, which would lead to a decrease in light yield. Additionally, one would observe a decrease in the triplet molecule lifetime. Work by Himi *et al.* suggests that an impurity level of 0.5 atoms of nitrogen per 10^6 atoms of argon in the liquid could decrease the observed triplet lifetime by as much as 0.1 μs [31]. Further experiments quantifying the reduction of the triplet lifetime due to nitrogen and oxygen impurities have recently been performed by the WARP Collaboration [32,33]. To avoid signal degradation, we continually circulate the argon through a getter before reliquefying it back into the detector. We use daily measurements of both the light yield and the triplet lifetime to monitor the purity level.

We measure the light yield in the manner described earlier in this section, and we use the same ^{57}Co data to measure the triplet lifetime. First, we select events in the 122-keV peak to make sure we use a similar data set for each individual measurement. The top and bottom PMT traces are normalized by the size of the single photoelectron and summed together. We align each pulse based on its estimated trigger time, defined as the time at which the trace first crosses 20% of its maximum value. At this trigger time, the relative time for each pulse is $t = 0$. Between 5000 and 10 000 traces are averaged, and the following model is fit to the average trace between 1 and 7 μs from the trigger:

$$\langle V(t) \rangle = A \exp(-t/\tau_l) + B, \tag{3}$$

where $\langle V(t) \rangle$ is the expected trace, A is a normalization factor, τ_l is the triplet lifetime, and B is an additional baseline term that helps stabilize the fit over a range of fit windows. An example fit is shown in Fig. 5.

We find two significant sources of systematic error in the fit parameters stemming from the voltage applied to the PMTs and the choice of fit window. Although we do not fully understand the PMT voltage effect, we estimate the systematic uncertainty to be 33 ns by changing the PMT voltages by $\pm$75 V (equivalent to dividing or multiplying the gain by 2). We do not fit the data before 1 μs or after 9 μs, as the fit becomes less reliable because of contamination from the fast component and baseline noise, respectively. We estimate the systematic uncertainty associated with the fit window to be about 35 ns by both varying the end time by $\pm$2 μs and fitting the data within 5 μs windows ending at 6, 7, and 8 μs from the trigger. We combine the two sources of error into a single systematic uncertainty estimate of 50 ns.

During the four months of operation, we measure the long time constant and signal yield to be $(1463 \pm 5_{\text{stat}} \pm 50_{\text{sys}})$ ns and (4.85 ± 0.08) photoelectrons/keVee. The uncertainty on

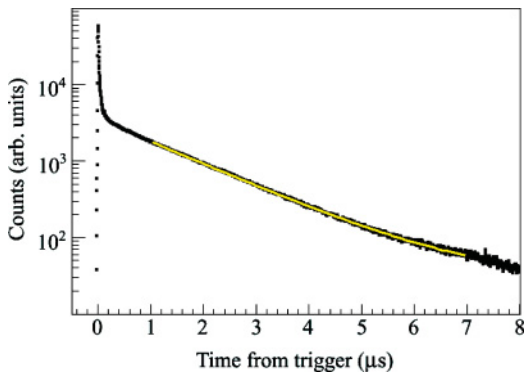

FIG. 5. (Color online) Example fit of a single exponential to an average trace to measure the long time constant in liquid argon.

the signal yield is statistical, and varying the PMT voltage by ±75 V has no apparent effect. For a fixed fit window and PMT voltage, the long time constant is stable to within 1%, while the signal yield is stable to within 5%.

III. EXPERIMENTAL RESULTS

A. Detection time PDF model

We measure the time dependence of scintillation light produced by electronic and nuclear recoil scattering events in our detector. For an event with energy deposited at time t_0, we model the temporal probability density functions (PDFs) for the emission times of scintillation photons as the weighted sum or mixture of two exponential PDFs:

$$f(t - t_0) = qg(t - t_0, \tau_l) + (1 - q)g(t - t_0, \tau_s), \quad (4)$$

where

$$g(t, \tau) = \frac{1}{\tau} \exp\left(\frac{-t}{\tau}\right), \quad (5)$$

τ_l and τ_s are the long and short time constants for both nuclear and electronic recoil event classes at any given energy, and the probability parameter q takes different values for the two classes of events.

At each PMT, detected scintillation photons yield photoelectrons that produce observed voltage traces. For the small detector in this experiment, scintillation transit times are negligible. We assume that the duration of energy deposition and excimer formation is instantaneous compared to the time scales relevant to scintillation light emission. Hence, we model the expected voltage trace as a convolution of the impulse response function of the PMT and the PDF model for the emission of scintillation photons:

$$\langle V(t) \rangle \propto \int_{s=t_*}^{\infty} h_V(t - s) f(s - t_*)\, ds, \quad (6)$$

where $h_V(t)$ is the impulse response function of the PMT, and t_* is an additional model parameter that relates the energy deposit time t_0 to the relative time scale we associate with our measurement of $h_V(t)$. We estimate the impulse response function by averaging single photoelectron events observed in our calibration data. Neglecting additive noise and other instrumental systematic errors, the integral of the voltage trace is proportional to the number of photoelectrons produced by the event.

The data are divided into 15 nonuniform bins by photoelectron number, with the smallest signal bin including events consisting of 20–24 photoelectrons and the largest bin including events consisting of 240–279 photoelectrons. These bins define the region of interest. For each photoelectron bin, we generate template traces for both electronic and nuclear recoils by averaging all events of a given type. The traces are averaged in the same manner as described in Sec. II C and normalized.

We use these average voltage traces to determine the model parameters: $\tau_l, \tau_s, q_{\text{nuclear}}$ and $q_{\text{electronic}}$. The observed and predicted fraction of a normalized trace in the ith time bin are called $p_m(i)$ and $\hat{p}(i)$, respectively. We obtain the model parameters by minizing the squared Matusita distance [34–36] between p_m and p:

$$|p - p_m|_M = \sum_i (\sqrt{p_m(i)} - \sqrt{\hat{p}(i)})^2, \quad (7)$$

where negative values of p_m are set to 0. For each bin, we fit our model to normalized mean voltage trace data in a time window that ends about 6800 ns after the trigger time. We determine t_* to be 30 ns before the trigger time, chosen to minimize the value of Eq. (7). Table II shows the estimated model parameters for each photoelectron bin. Figure 6 shows the model prediction along with data for the 80–99 photoelectron bin.

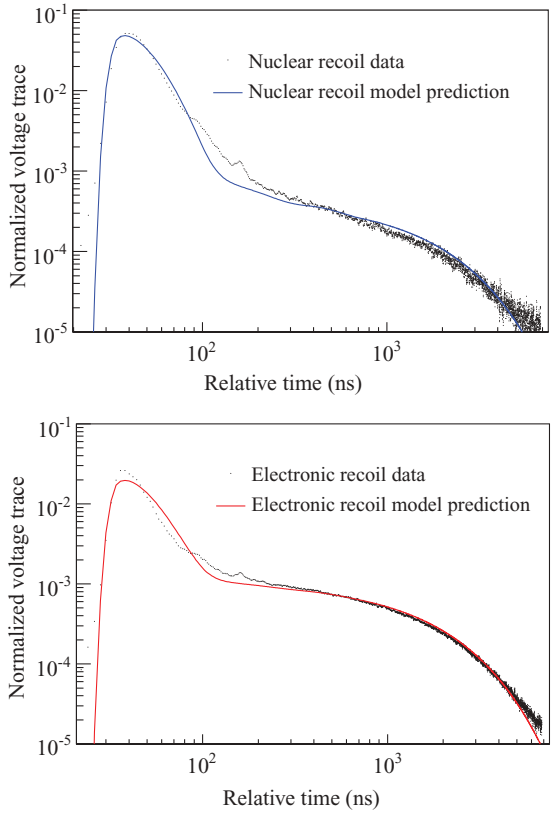

FIG. 6. (Color online) Observed and predicted mean voltage traces for nuclear and electronic recoil events of 80–99 photoelectrons.

Between 80 and 300 ns, there is a feature in both event classes that is not well predicted by the model. A scintillation component that decays as approximately t^{-1} has been observed in liquid helium, attributed to diffusion-dominated excimer-excimer destruction [11]. When we fit a model including the full form of this component as described in Ref. [11], the parameter estimates are not well determined. Previous observations of scintillation in argon have noted an intermediate exponential component with a decay time of 20–40 ns [9]. Unfortunately, a model that includes a third exponential component neither returns stable model parameters as a function of energy nor accurately predicts the trace behavior between 80 and 300 ns, so we prefer the two-component model. We assume that the sharp bump localized at 150 ns is caused by the cabling and electronics.

TABLE II. Estimated model parameters and 1-σ uncertainties for each photoelectron bin. The systematic errors described in the text are the dominant source of error.

Bin (pe)	τ_l (ns)	τ_s (ns)	q_{nuclear}	$q_{\text{electronic}}$
20–24	1634 ± 150	9 ± 3	0.378 ± 0.011	0.523 ± 0.015
25–29	1535 ± 128	10 ± 3	0.382 ± 0.011	0.573 ± 0.015
30–34	1478 ± 107	10 ± 3	0.357 ± 0.010	0.601 ± 0.014
35–39	1455 ± 102	11 ± 3	0.353 ± 0.010	0.627 ± 0.014
40–49	1461 ± 96	12 ± 3	0.344 ± 0.010	0.658 ± 0.014
50–59	1459 ± 92	12 ± 3	0.327 ± 0.009	0.681 ± 0.015
60–69	1439 ± 89	12 ± 3	0.315 ± 0.010	0.699 ± 0.015
70–79	1448 ± 89	13 ± 3	0.309 ± 0.010	0.710 ± 0.015
80–99	1447 ± 85	13 ± 3	0.298 ± 0.010	0.721 ± 0.015
100–119	1452 ± 84	13 ± 3	0.289 ± 0.010	0.733 ± 0.015
120–139	1447 ± 84	13 ± 3	0.284 ± 0.011	0.741 ± 0.016
140–159	1446 ± 84	14 ± 3	0.278 ± 0.012	0.747 ± 0.016
160–199	1450 ± 84	14 ± 3	0.272 ± 0.013	0.752 ± 0.016
200–239	1460 ± 84	15 ± 3	0.265 ± 0.015	0.760 ± 0.016
240–279	1467 ± 84	15 ± 3	0.258 ± 0.018	0.764 ± 0.016

We determine 1-σ random uncertainties for the model parameters with a nonparametric bootstrap resampling scheme [37]. A rigorous quantification of systematic uncertainty arising from the fit window, the voltage applied to the PMT, and variation in the response of each individual PMT is difficult. Nonetheless, we get approximate estimates of systematic uncertainties from these sources, and these systematics are the dominant source of error. We estimate 1-σ systematic uncertainties in the parameters τ_i (for $i = l, s$) as $0.5 \times (\tau_{i,\max} - \tau_{i,\min})$, where $\tau_{i,\max}$ and $\tau_{i,\min}$ are the maximum and minimum values taken by τ_i for different choices of time windows. We refit the model to data using time windows of approximately 5000 and 8600 ns from the trigger time and vary the offset parameter t_* by ± 2 ns. We also check for differences between the response of each PMT in five different photoelectron bins. We include the voltage-dependent errors described in Sec. II C in the systematic uncertainty of τ_l, and we estimate the voltage-dependent systematic variation of the q values. We find that the time constants are most influenced by choice of fit window, while the q values are most influenced by PMT effects. We combine all sources of error to obtain the estimates of systematic uncertainty shown in Table II.

As a consistency check on the quality of fit, for each photoelectron bin we use our model to predict the prompt fraction, a discrimination statistic described in detail in the next section. We compute the difference between the predicted and observed prompt fractions, and the root-mean-square values of this prediction error across all bins are, respectively, 0.007 and 0.003 for the nuclear and electronic recoil event classes. The fractional root-mean-square value of this prediction error is about 1% for both event classes.

B. Prompt fraction method

The prompt fraction method is a simple approach to pulse shape discrimination. For each trace, we define the prompt fraction f_p as

$$f_p = \frac{\int_{T_i}^{\xi} V(t)\,dt}{\int_{T_i}^{T_f} V(t)\,dt}, \tag{8}$$

where $V(t)$ is the voltage trace from the PMT, ξ is an integration time determined to optimize the ERC, $T_i = t_0 - 50$ ns, $T_f = t_0 + 9$ μs, and t_0 is the trigger time as defined in Sec. II B. The measured discrimination does not significantly improve by extending T_f to 20 μs. Figure 7 shows a scatter plot of f_p versus energy for both electronic and nuclear recoils. The two populations of events represent the tagged data remaining in the neutron generator data set and the ^{22}Na data set after the selection cuts described in Sec. II B have been made. We choose $\xi = 90$ ns by estimating the ERC based on a simple Gaussian model for values of ξ from 50 to 250 ns over a variety of different photoelectron bins. Although the value of ξ has only a weak effect on the predicted discrimination, a choice of $\xi = 90$ ns provides the best results across the widest range of energies in the region

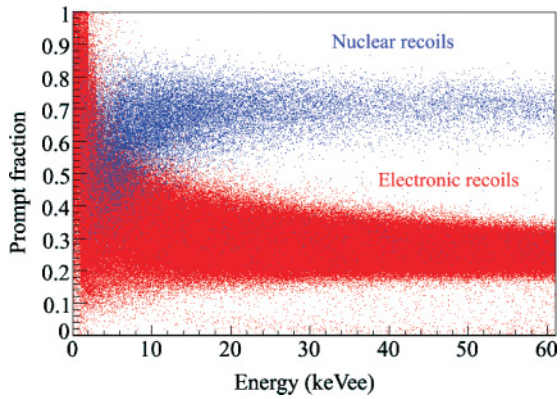

FIG. 7. (Color online) Scatter plot of f_p vs energy for tagged electronic and nuclear recoils, where $\xi = 90$ ns.

TABLE III. Estimated mean values of f_p vs energy, where $\xi =$ 90 ns. The main sources of uncertainty are systematic, stemming from voltage effects and differences in the measured signals between the two PMTs.

Energy (keVee)	$\hat{f}_{p,\text{electronic}}$	$\hat{f}_{p,\text{nuclear}}$
5–6	0.391 ± 0.012	0.566 ± 0.018
6–7	0.376 ± 0.011	0.595 ± 0.018
7–8	0.361 ± 0.011	0.607 ± 0.019
8–9	0.349 ± 0.011	0.625 ± 0.019
9–10	0.339 ± 0.010	0.638 ± 0.020
10–11	0.334 ± 0.010	0.640 ± 0.020
11–12	0.328 ± 0.010	0.649 ± 0.020
12–13	0.322 ± 0.010	0.663 ± 0.020
13–14	0.319 ± 0.010	0.658 ± 0.020
14–15	0.314 ± 0.009	0.675 ± 0.020
15–16	0.311 ± 0.009	0.683 ± 0.021
16–17	0.309 ± 0.009	0.678 ± 0.021
17–18	0.304 ± 0.009	0.685 ± 0.021
18–19	0.302 ± 0.009	0.682 ± 0.021
19–20	0.299 ± 0.009	0.684 ± 0.021
20–21	0.297 ± 0.009	0.690 ± 0.021
21–22	0.295 ± 0.009	0.695 ± 0.021
22–23	0.292 ± 0.009	0.699 ± 0.021
23–24	0.290 ± 0.009	0.690 ± 0.021
24–25	0.288 ± 0.009	0.688 ± 0.021
25–26	0.289 ± 0.009	0.695 ± 0.021
26–27	0.288 ± 0.009	0.696 ± 0.021
27–28	0.285 ± 0.009	0.696 ± 0.021
28–29	0.284 ± 0.009	0.701 ± 0.021
29–30	0.283 ± 0.009	0.708 ± 0.021
30–31	0.281 ± 0.009	0.701 ± 0.021
31–32	0.282 ± 0.009	0.689 ± 0.021

of interest, and that value is used for the analysis presented in this paper.

For energy bins of width 1 keVee between 5 and 32 keVee, we form histograms of the electronic and nuclear recoil f_p statistics. To estimate the expected value of f_p, $\hat{f}_p$, we fit a Gaussian function to the empirical distributions. In Table III and Fig. 8, we present the estimated mean f_p for both

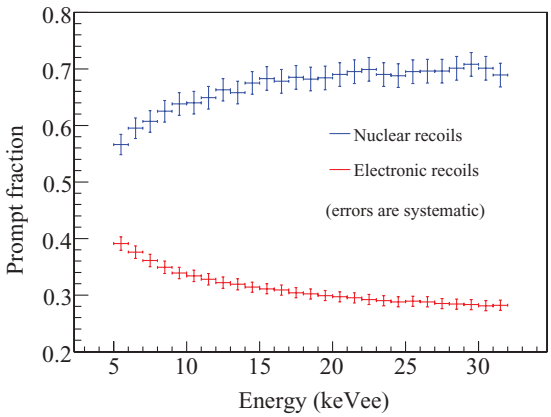

FIG. 8. (Color online) Estimated mean f_p vs energy for both event classes, where $\xi = 90$ ns.

classes of events in the energy range of interest. We estimate the systematic uncertainty on the values in Table III to be 3%. This uncertainty estimate comes from changing the PMT voltage by -75 V and from variations in the measured signals between the two PMTs. The mean values of the f_p distributions for the two event classes are closer at low energies than at high energies, possibly because dE/dx for nuclear recoils decreases at low energies while it increases for electronic recoils. Therefore, the PSD improves at higher energies both because of increased photoelectron statistics and because of increased separation between the mean f_p values.

We estimate the ERC as the number of tagged electronic recoil events with $f_p > \hat{f}_{p,\text{nuclear}}$ divided by the total number of electronic recoil events, where $\hat{f}_{p,\text{nuclear}}$ is the estimated mean f_p for nuclear recoils of that energy. This restriction sets a nuclear recoil acceptance level of approximately 50%. Since the shielding, coincidence, and timing cuts do not eliminate all neutron backgrounds in the detector, a background estimation N_{bg} is made by measuring the rate of background neutrons R_{bgn} and assuming that the background is dominated by these neutrons hitting in accidental coincidence with γ rays (R_γ) in the liquid scintillator during the time allowed by the time-of-flight cut:

$$N_{\text{bg}} = R_{\text{bgn}} \times R_\gamma \times \text{TOF} \times T_a, \tag{9}$$

where T_a is the acquisition time of the data. To enable comparison with the measured ERC, we divide N_{bg} for each energy bin by the total number of electronic recoil events in that bin.

Figure 9 shows the ERC observed using the prompt fraction method. We also plot the background estimation, two PSD projections based on the statistical model described below, and the ERC observed by applying a multibin method of PSD described in the next section. We convert the energy axis in Fig. 9 to keV of nuclear recoil energy (keVr) from keVee by dividing all electron equivalent energies by a constant nuclear

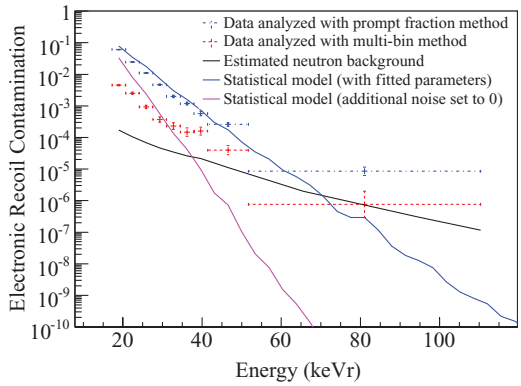

FIG. 9. (Color online) Measured electronic recoil contamination obtained by using the prompt fraction method and the multibin method. Also shown are the background estimation and model predictions described in the text. We include a model with the additional noise set to 0 for comparison. No contamination events above 69 keVr were observed by use of either method. The energy axis has been scaled from keVee to keVr by use of a constant nuclear recoil scintillation efficiency of 0.29 as discussed in the text.

recoil scintillation efficiency of 0.29. This value was obtained by measurements using the same apparatus described in this paper and will be discussed in an upcoming publication [38]. We present the PSD results in keVr because that is the unit of interest for a dark matter detector. Using the prompt fraction method, for a nuclear recoil acceptance level of approximately 50%, we measure a background- and statistics-limited level of ERC in our detector of 8.5×10^{-6} between 52 and 110 keVr (11 contamination events). We observe no nuclear recoil-like events above 69 keVr. For comparison, there is an uncorrelated neutron background rate of ~ 6 mHz between 69 and 110 keVr, corresponding to 0.25 expected background counts in that energy range.

Following work done by the DEAP Collaboration [39,40], we model our estimates of the number of photoelectrons in the prompt and late time windows, N_p and N_l, as normally distributed, independent random variables with means μ_p and μ_l and variances σ_p^2 and σ_l^2. The estimated total number of photoelectrons, $N_{\text{tot}} = N_p + N_l$, is also a random variable, with mean $\mu_{\text{tot}} = \mu_p + \mu_l$ and variance $\sigma_{\text{tot}}^2 = \sigma_p^2 + \sigma_l^2$. We express μ_p and μ_l in terms of μ_{tot} and $\hat{f}_p$, and we decompose the variances into two components:

$$\begin{aligned} \mu_p &= \hat{f}_p \mu_{\text{tot}}, \\ \mu_l &= (1 - \hat{f}_p)\mu_{\text{tot}}, \\ \sigma_p^2 &= \mu_p + \sigma_{p,\text{add}}^2, \\ \sigma_l^2 &= \mu_l + \sigma_{l,\text{add}}^2, \end{aligned} \tag{10}$$

where $\sigma_{p,\text{add}}$ and $\sigma_{l,\text{add}}$ represent additional sources of random variability beyond what we expect from Poisson counting statistics (for example, integration noise).

Hinkley [41] has described in detail the probability density function of the ratio of two normally distributed, correlated random variables. For simplicity, we present here an approximation [given by Eq. (9) of Ref. [41]] to the PDF of $f_p = N_p/N_{\text{tot}}$:

$$\begin{aligned} g_{f_p}(x) = {} & \frac{\sigma_l^2 \mu_p x + \sigma_p^2 \mu_l (1-x)}{\sqrt{2\pi}\left[\sigma_l^2 x^2 + \sigma_p^2 (1-x)^2\right]^{3/2}} \\ & \times \exp\left[-\frac{\mu_l x - \mu_p (1-x)^2}{2\left[\sigma_l^2 x^2 + \sigma_p^2 (1-x)^2\right]} \right], \end{aligned} \tag{11}$$

where we have used the fact that the correlation ρ between N_p and N_{tot} is

$$\rho = \frac{\sigma_p}{\sqrt{\sigma_p^2 + \sigma_l^2}}. \tag{12}$$

For the analysis below, we use the exact PDF [Eq. (1) in Ref. [41]], although in practice the approximation is extremely good down to the lowest energy bin examined.

We fit the electronic recoil data with the statistical model in each energy bin by fixing N_{tot} according to our measured light yield and treating $\hat{f}_p$, $\sigma_{p,\text{add}}$, and $\sigma_{l,\text{add}}$ as free parameters. We assume that the statistical distribution of f_p does not strongly depend on the value of N_{tot} for events of the same energy. For any particular energy deposit, N_{tot} is a random variable, and events due to many different energy deposits can contribute to prompt ratio data in any one bin in N_{tot} space. The probability density function for prompt ratio data is a mixture of energy-dependent PDFs, and we neglect this energy blurring effect. Simple Monte Carlo studies suggest that the ratio-of-Gaussians model breaks down for idealized Gaussian data as a result of the constraint on N_{tot} resulting from the binning of data, and this effect has not been taken into account in our analysis.

We use the statistical model to estimate the expected fraction of electronic recoils that are misclassified as nuclear recoils:

$$\text{ERC} = \int_{\eta}^{1} g_{f_p}(x)\, dx. \tag{13}$$

Here, we choose $\eta = \hat{f}_{p,\text{nuclear}}$ to set the nuclear recoil acceptance level to approximately 50%, and we choose the parameters of g_{f_p} according to the fits to the electronic recoil f_p distribution. Figure 9 shows the predicted ERC versus energy according to this model. We also plot the idealized case where $\sigma_{l,\text{add}}$ and $\sigma_{p,\text{add}}$ are set to 0. In general, we expect that the normal distribution model for N_p and N_l is an approximation for any energy of interest. For the idealized case where $\sigma_{p,\text{add}} = \sigma_{l,\text{add}} = 0$, N_p and N_l would be Poisson random variables rather than Gaussian random variables. Hence, the ERC predicted by the ratio-of-Gaussians model for the idealized case should be interpreted with caution particularly at lower energies where the accuracy of a normal distribution model for a Poisson random variable can be very poor.

Figure 10 shows an example of the model fit for 14–15 and 30–31 keVee electronic recoil events. There is a deviation from the model at low f_p values that we attribute to pile-up and noise triggers. There is also an excess of events in the high f_p region. This excess might be caused by edge effects in our detector coming from γ tracks going into the walls or the TPB layer, producing extra prompt light. A larger detector with position reconstruction capability might be able to eliminate such edge effects. Some unknown phenomena could be at work in the production and decay of argon molecular states, yielding a small fraction of events with anomalously large f_p values. A third possibility is approximation error stemming from incorrect model assumptions, such as the Gaussianity of N_p and N_l or the effect of data binning. These possible effects can be better investigated by detectors with improved neutron shielding, and future studies will require more work to better calibrate the ERC predictions made by the ratio-of-Gaussians model.

Figure 11 shows the fitted values of the variances $\sigma_l^2 = \mu_l + \sigma_{l,\text{add}}^2$ and $\sigma_p^2 = \mu_p + \sigma_{p,\text{add}}^2$ versus the estimated number of photoelectrons in μ_l and μ_p. The ideal case of zero additional noise ($\sigma^2 = \mu$) has been shown for comparison. The relationship between the estimated variance parameters and the corresponding estimates of the number of photoelectrons is approximately linear, suggesting that $\sigma_{l,\text{add}}^2$ and $\sigma_{p,\text{add}}^2$ are proportional to μ_l and μ_p. Straight line fits to the late and prompt variances have slopes of 2.2 and 1.3, respectively. Because of the various uncertainties in the fit such as that associated with data binning, these numbers do not represent

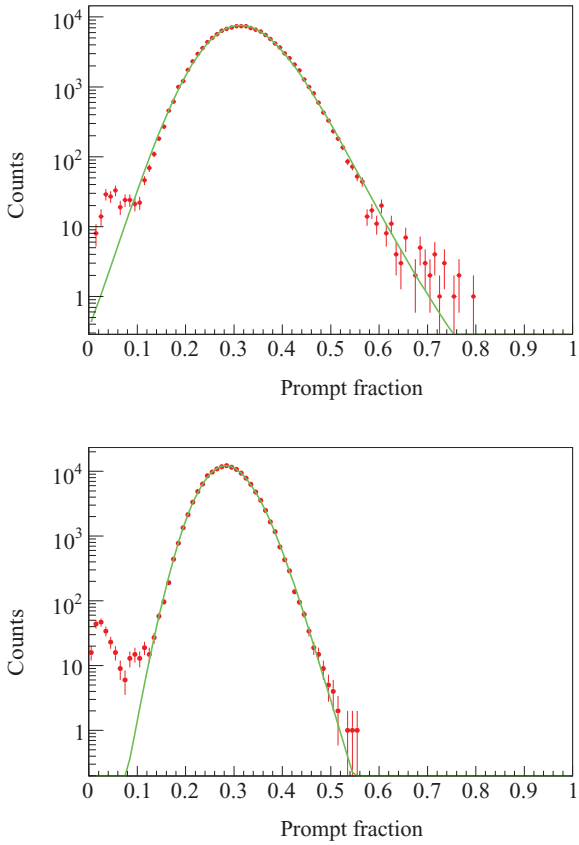

FIG. 10. (Color online) Projections of the electronic recoil data from Fig. 7 onto the y axis for 14–15 keVee (top) and 30–31 keVee (bottom) events, fitted by Eq. (11) as discussed in the text.

a rigorous estimate of the amount of noise in the late and prompt distributions; however, they might be used as a point of comparison with future detectors in trying to reduce the overall noise in the system. Possible sources of this additional noise include integration noise, the widths of the single photoelectron spectra, and variability in the prompt window size arising from uncertainty in the determined trigger position. To improve PSD, future experiments will need to reduce the size of this additional noise to approach the ideal case.

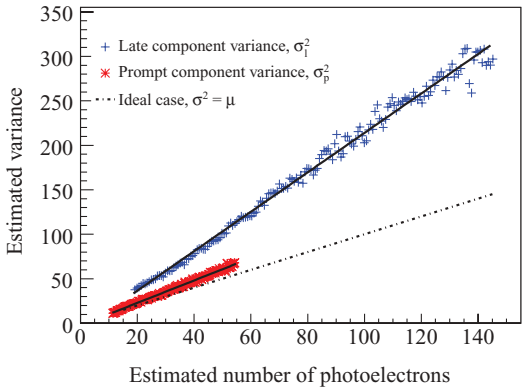

FIG. 11. (Color online) Estimated σ_l^2 and σ_p^2 parameters from the statistical model plotted against the estimated number of photoelectrons in the late and prompt components, respectively. Each distribution is fitted by a straight line, and the ideal case where $\sigma^2 = \mu$ is also shown.

C. Multibin method

The prompt fraction method of PSD is based on binning the voltage trace into two time bins. We generalize this approach by representing a normalized voltage trace as a $K \times L$ dimensional matrix. In this representation, we categorize the data by the number of photoelectrons in the event, and L refers to this division of data into photoelectron bins. We also partition the voltage trace into K time bins. We choose $K = 10$ for ease of computation, but there may be a better choice of K. With the exception of the four smallest signal bins, which have been combined to form bins of 20–29 and 30–39 photoelectrons, we use the same average voltage traces obtained in Sec. III A as templates.

We partition each template into $K = 10$ time bins. The upper and lower endpoints of each time bin are selected so that the fractions of the template trace for 80–99 photoelectron electronic recoil events that fall in each time bin are approximately equal. The initial bin starts 50 ns before the trigger, and the endpoints of each bin are as follows, measured in nanoseconds from the trigger: 8, 18, 56, 200, 440, 750, 1180, 1800, 2950, and 8000. We do not adjust these endpoints for different photoelectron numbers but use the 80–99 photoelectron based time binning scheme for all cases.

The kth component of the normalized template for an event that falls in the lth photoelectron bin for the nuclear and electronic recoil classes is denoted $p_n(k, l)$ or $p_e(k, l)$, respectively. For instance, $p_n(1, 1)$ represents the fraction of the 20–29 photoelectron nuclear recoil template trace that falls in the first time bin (between 50 ns before the trigger and 8 ns after the trigger).

To assign an event to either the nuclear recoil or electronic recoil class, we first compute a discrimination statistic for the event. We motivate a discrimination statistic based on analysis of an idealized experiment in which we could observe the absolute detection time of each photoelectron without error. In this ideal case, for a fixed number of detected photoelectrons, the observed number of photoelectrons in the time bins is a multinomial random variable.

Given that the fraction of detected photoelectrons in the kth bin is $p_m(k, l)$, the multinomial log-likelihood statistics for the nuclear and electronic recoil classes are

$$\ln Y_n = N_{\text{tot}} \sum_{k=1}^{K} \sum_{l=1}^{L} \delta_{ll'} p_m(k, l) \ln p_n(k, l') + \text{const}, \qquad (14)$$

and

$$\ln Y_e = N_{\text{tot}} \sum_{k=1}^{K} \sum_{l=1}^{L} \delta_{ll'} p_m(k, l) \ln p_e(k, l') + \text{const}, \qquad (15)$$

respectively [42]. Here, N_{tot} is the total number of detected photoelectrons, and $p_n(k, l)$ and $p_e(k, l)$ are the expected values of the fraction of detected photoelectrons in the kth time bin for the nuclear and electronic recoil classes, respectively.

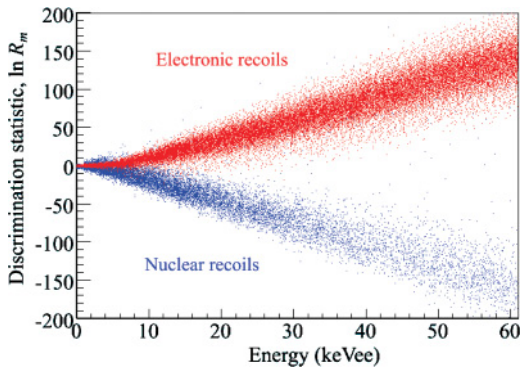

FIG. 12. (Color online) Scatter plot of ln R_m vs energy for both electronic and nuclear recoils.

For this idealized case, a natural choice for the discrimination statistic is the log-likelihood ratio statistic

$$\ln R_m = \ln Y_e - \ln Y_n. \tag{16}$$

In our experiment, the observed data are not multinomial, primarily because we observe a noisy voltage waveform rather than discrete detection times. Nonetheless, we compute a discrimination statistic using Eqs. (14)–(16), where we estimate N_{tot} and $p_m(k,l)$ from any voltage trace of interest and determine $p_e(k,l)$ and $p_n(k,l)$ as described earlier.

Figure 12 shows a scatter plot of ln R_m versus energy, analogous to Fig. 7. From this point, the analysis parallels the prompt fraction method, as we form histograms of ln R_m by energy bin and fit a Gaussian function to the observed ln R_m statistics to estimate the mean of ln R_m. Figure 13 shows an example of the fitted projections for 14–15 and 30–31 keVee events.

For each energy bin, we estimate the mean values of ln R_m for nuclear recoils based on the Gaussian fits to the observed distributions, and this estimated mean value determines an approximate 50% nuclear acceptance threshold. We then determine the fraction of events in the electronic recoil data set that have discrimination statistics less than this mean value to determine the observed level of ERC using the multibin method. If we determine the 50% nuclear acceptance threshold by finding the median values of the nuclear recoil distributions, the observed ERC is not significantly affected. Figure 9 in Sec. III B shows the ERC using the multibin method. The multibin method outperforms the prompt fraction method by as much as an order of magnitude. For a nuclear recoil acceptance of approximately 50%, we have measured a background- and statistics-limited ERC of 7.6×10^{-7} between 52 and 110 keVr (1 contamination event). We observe no contamination events above 62 keVr using the multibin method.

IV. MAXIMUM LIKELIHOOD PSD

We predict the PSD achievable in a large detector with many PMTs by assuming we can measure discrete times for each photoelectron detected in an event. We simulate events in this detector using the PDFs measured in Sec. III A and assume that the detection times of photoelectrons are measured

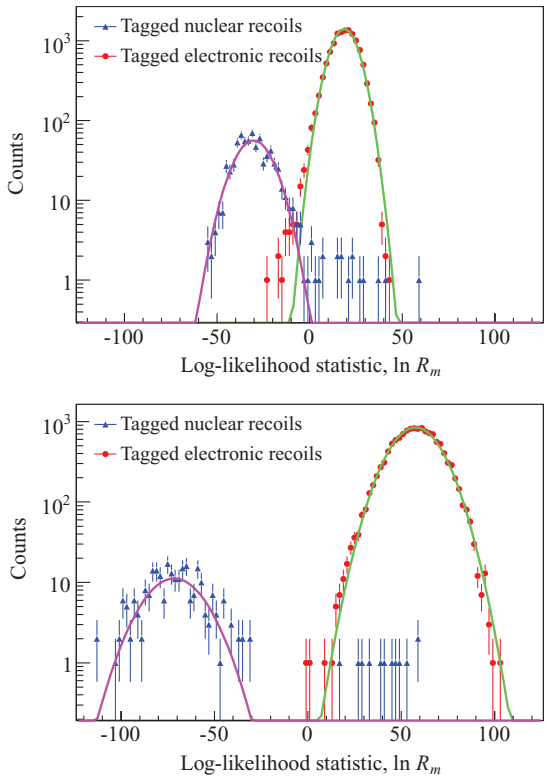

FIG. 13. (Color online) Projections of Fig. 12 onto the y axis for 14–15 keVee (top) and 30–31 keVee (bottom) events, with Gaussian fits to both the electronic (left) and nuclear (right) recoil distributions.

without error. We develop a maximum likelihood PSD method and apply it to the simulated data.

For an event that generates N photoelectrons, we denote the detection times as $\mathbf{t} = (t_1, t_2, \ldots, t_N)$. We define the log-likelihood function ln L of these data following Ref. [43] as

$$\ln L = -m + \sum_{i=1}^{N} \ln[r_{\text{bg}} + \lambda f(t - t_0)], \tag{17}$$

where

$$m = \int_{T_b}^{T_e} [r_{\text{bg}} + \lambda f(t - t_0)]\, dt, \tag{18}$$

t_0 is the time at which the energy deposit occurs, $f(t - t_0)$ is the PDF for the observed photoelectrons [Eq. (4)], λ is the expected number of detected photoelectrons generated by the event, T_b and T_e are the start and end time of the observation, and r_{bg} is the background rate.

In our simulations, we set $r_{\text{bg}} = 0$ and $t_0 > T_b$. The maximum likelihood estimates of t_0 and λ are therefore t_1, the first detection time, and $\hat{\lambda}$, where

$$\hat{\lambda} = \frac{N}{q F(T_e - t_1, \tau_1) + (1 - q) F(T_e - t_1, \tau_2)} \tag{19}$$

and $F(T, \tau) = 1 - \exp(-T/\tau)$. Consequently, $m = N$. Additionally, the time window in our simulations is 40 μs, so $\int_{T_b}^{T_e} f(t - t_0)\, dt \approx 1$. Thus, for our case, the likelihood

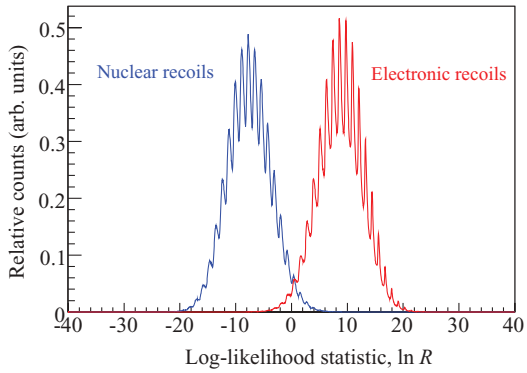

FIG. 14. (Color online) Monte Carlo estimates of the log-likelihood statistics for events that yield 50 photoelectrons.

function of the observed data is well approximated as

$$L(\mathbf{t}) \approx \exp(-N)\, N^N \prod_{i=1}^{N} f(t_i - t_1). \tag{20}$$

Following Ref. [13] and the discussion above, for each simulated event we determine $L(\mathbf{t})$ for both the electronic and nuclear recoil event classes as modeled in Sec. III A. These values are denoted $L_e(\mathbf{t})$ and $L_n(\mathbf{t})$. We define the log-likelihood ratio $\ln R$ as

$$\ln R = \ln L_e(\mathbf{t}) - \ln L_n(\mathbf{t}). \tag{21}$$

Figure 14 shows this log-likelihood statistic for simulated electronic and nuclear recoil events that yield 50 photoelectrons. The event is assigned to the nuclear recoil class if $\ln R$ is less than an adjustable threshold that can be varied to increase the discrimination against electronic recoils at the cost of decreasing nuclear recoil acceptance. The Monte Carlo estimate of the distribution of $\ln R$ has prominent ripples, even though the Monte Carlo estimates of L_n and L_e do not. In our Monte Carlo study, we simulate events that yield a fixed number of photoelectrons according to PDFs with the assumption of perfect knowledge. Furthermore, we neglect dark current noise. In an actual experiment, we expect that imperfect energy resolution due to variability in counting statistics and dark current effects would attenuate the ripples in the $\ln R$ distribution.

To illustrate the maximum likelihood method, we simulate a detector with a signal yield of 6 photoelectrons/keVee, as might be possible in a detector with full PMT coverage. We neglect dark current and we set the discrimination threshold to accept 50% of nuclear recoils. For comparison, we simulate prompt fraction data by assuming the number of prompt photoelectrons is a binomial random variable with an expected value determined by the measured PDFs, and the total number of photoelectrons is assumed to be known without error. This idealized binomial model predicts a much lower ERC than the statistical model discussed in Sec. III B.

The maximum likelihood discrimination method outperforms the idealized prompt fraction method, as shown in Fig. 15. We also expect that the maximum likelihood method will be more robust than the prompt fraction method to

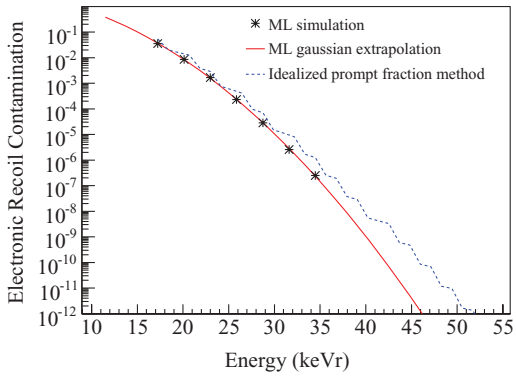

FIG. 15. (Color online) Predicted performance of maximum likelihood and prompt ratio PSD methods for a detector yielding 6 photoelectrons/keVee (the energy axis has been scaled from keVee to keVr by use of a constant nuclear recoil scintillation efficiency of 0.29 as discussed in Sec. III B).

background noise. For the prompt fraction case, we select a threshold in prompt photoelectron space to yield a nuclear recoil acceptance probability as close to 0.5 as possible. Because of quantization effects, the actual nuclear recoil acceptance probability varies by about 0.5, and sawtooth-like artifacts occur in the prompt fraction ERC curve shown in Fig. 15.

V. CONCLUSION

Using a detector with a signal yield of 4.85 photoelectrons/keVee, we measured the scintillation time dependence of electronic and nuclear recoils in liquid argon down to 5 keVee or 20 keVr. We developed a prompt fraction method of PSD in liquid argon, and for a nuclear recoil acceptance level of 50%, we measured a background- and statistics-limited level of ERC to be 8.5×10^{-6} between 52 and 110 keVr with no contamination events above 69 keVr. We also developed a multibin method of PSD, improving on the prompt fraction method by as much as an order of magnitude. With this method, we measured a background- and statistics-limited level of ERC of 7.6×10^{-7} between 52 and 110 keVr for the same nuclear recoil acceptance of 50%. We modeled the observed prompt fraction data as the ratio of two normally distributed, correlated random variables, where we assumed N_p and N_l are uncorrelated; we discussed discrepancies between observed and predicted prompt fraction results. Finally, we developed a maximum likelihood method of PSD for a detector capable of measuring a discrete detection time for each observed photoelectron in an event.

ACKNOWLEDGMENTS

We thank M. Boulay, C. Jillings, B. Cai, and J. Lidgard for useful discussions and for developing the ratio-of-Gaussians model used in this analysis. We acknowledge S. Seibert and J. Klein for their contributions to the Monte Carlo simulations software package. This work was supported by the David and Lucille Packard Foundation, the Los Alamos Directed Research and Development Program, and the US Department of Energy.

[1] For a review, see G. Jungman, M. Kamionkowski, and K. Griest, Phys. Rep. **267**, 195 (1996).

[2] Z. Ahmed, D. S. Akerib, S. Arrenberg, M. J. Attisha, C. N. Bailey, L. Baudis, D. A. Bauer, J. Beaty, P. L. Brink, T. Bruch, *et al.*, arXiv:0802.3530v2 [astro-ph] (2008).

[3] J. Angle, E. Aprile, F. Arneodo, L. Baudis, A. Bernstein, A. Bolozdynya, P. Brusov, L. C. C. Coelho, C. E. Dahl, L. DeViveiros *et al.*, Phys. Rev. Lett. **100**, 021303 (2008).

[4] E. Aprile, K. L. Giboni, P. Majewski, K. Ni, M. Yamashita, R. Gaitskell, P. Sorensen, L. DeViveiros, L. Baudis, A. Bernstein *et al.*, New Astron. Rev. **49**, 289 (2005).

[5] D. B. Cline, Y. Seo, F. Sergiampietri, H. Wang, J. T. White, J. Gao, P. Picchi, G. Mannocchi, L. Periale, F. Pietropaolo *et al.*, Nucl. Phys. B, Proc. Suppl. **124**, 229 (2003).

[6] A. Rubbia, Nucl. Phys. B, Proc. Suppl. **149**, 197 (2005).

[7] R. Brunetti, E. Calligarich, M. Cambiaghi, F. Carbonara, A. Cocco, C. De Vecchi, R. Dolfini, A. Ereditato, G. Fiorillo, and L. Grandi, New Astron. Rev. **49**, 265 (2005).

[8] S. Kubota, M. Hishida, and A. Nohara, Nucl. Instrum. Methods **150**, 561 (1978).

[9] A. Hitachi, T. Takahashi, N. Funayama, K. Masuda, J. Kikuchi, and T. Doke, Phys. Rev. B **27**, 5279 (1983).

[10] J. A. Nikkel, R. Hasty, W. H. Lippincott, and D. N. McKinsey, Astropart. Phys. **29**, 161 (2008).

[11] D. N. McKinsey, C. R. Brome, S. N. Dzhosyuk, R. Golub, K. Habicht, P. R. Huffman, E. Korobkina, S. K. Lamoreaux, C. E. H. Mattoni, A. K. Thompson *et al.*, Phys. Rev. A **67**, 062716 (2003).

[12] D. Akimov, A. Bewick, D. Davidge, J. Dawson, A. S. Howard, I. Ivaniouchenkov, W. G. Jones, J. Joshi, V. A. Kudryavtsev, T. B. Lawson *et al.*, Phys. Lett. **B524**, 245 (2002).

[13] G. J. Davies, J. D. Davies, J. D. Lewin, P. F. Smith, and W. G. Jones, Phys. Lett. **B320**, 395 (1994).

[14] D. N. McKinsey and K. J. Coakley, Astropart. Phys. **22**, 355 (2005).

[15] M. G. Boulay and A. Hime, Astropart. Phys. **25**, 179 (2006).

[16] P. Benetti, F. Calaprice, E. Calligarich, M. Cambiaghi, F. Carbonara, F. Cavanna, A. G. Cocco, F. Di Pompeo, N. Ferrari, G. Fiorillo *et al.*, Nucl. Instrum. Methods Phys. Res., Sect. A **574**, 83 (2007).

[17] H. H. Loosli and H. Oeschger, Earth Planet. Sci. Lett. **7**, 67 (1969).

[18] J. A. Formaggio and C. J. Martoff, Annu. Rev. Nucl. Part. Sci. **54**, 361 (2004).

[19] P. Benetti, R. Acciarri, F. Adamo, B. Baibussinov, M. Baldo-Ceolin, M. Belluco, F. Calaprice, E. Calligarich, M. Cambiaghi, F. Carbonara *et al.*, Astropart. Phys. **28**, 495 (2008).

[20] M. G. Boulay and A. Hime, in Fifth Workshop on Science and Experiments for SNOLAB, 2006 (unpublished).

[21] Hamamatsu R5912-MOD02, www.hamamatsu.com.

[22] O. Cheshnovsky, B. Raz, and J. Jortner, J. Chem. Phys. **57**, 4628 (1972).

[23] D. N. McKinsey, C. R. Brome, J. S. Butterworth, R. Golub, K. Habicht, P. R. Huffman, S. K. Lamoreaux, C. E. H. Mattoni, and J. M. Doyle, Nucl. Instrum. Methods Phys. Res., Sect. B **132**, 351 (1997).

[24] Tectra Mini-Coater, www.tectra.de/mico.htm.

[25] Cryomech Model PT805, www.cryomech.com.

[26] Omni Nupure III, www.nupure.com.

[27] R. Brun and F. Rademakers, Nucl. Instrum. Methods Phys. Res., Sect. A **389**, 81 (1997).

[28] Thermo Electron Model MP320, www.thermo.com.

[29] S. Agostinelli, J. Allison, K. Amako, J. Apostolakis, H. Araujo, P. Arce, M. Asai, D. Axen, S. Banerjee, G. Barrand *et al.*, Nucl. Instrum. Methods Phys. Res., Sect. A **506**, 250 (2003).

[30] Reactor Analysis Tool, http://nu.ph.utexas.edu/rat/trac.

[31] S. Himi, T. Takahashi, J. Ruan, and S. Kubota, Nucl. Instrum. Methods **203**, 153 (1982).

[32] R. Acciarri, M. Antonello, B. Baibussinov, M. Baldo-Ceolin, P. Benetti, F. Calaprice, E. Calligarich, M. Cambiaghi, N. Canci, F. Carbonara *et al.*, arXiv:0804.1222v1 [nucl-ex], (2008).

[33] R. Acciarri, M. Antonello, B. Baibussinov, M. Baldo-Ceolin, P. Benetti, F. Calaprice, E. Calligarich, M. Cambiaghi, N. Canci, F. Carbonara *et al.*, arXiv:0804.1217v1 [nucl-ex], (2008).

[34] K. Matusita, Ann. I. Stat. Math. **5**, 59 (1954).

[35] W. R. Dillon and M. Goldstein, J. Am. Stat. Assoc. **73**, 305 (1978).

[36] M. Goldstein and W. Dillon, *Discrete Discrimination Analysis* (Wiley, New York, 1978).

[37] B. Efron and R. J. Tibshirani, *An Introduction to the Bootstrap* (Wiley, New York, 1993).

[38] D. Gastler, A. Hime, E. Kearns, W. H. Lippincott, D. N. McKinsey, D. Mei, J. A. Nikkel, and L. C. Stonehill, Phys. Rev. C, to be submitted.

[39] J. Lidgard, Masters thesis, Queens University, Canada, 2008.

[40] M. Boulay *et al.*, to be submitted.

[41] D. V. Hinkley, Biometrika **56**, 635 (1969).

[42] A. M. Mood, F. A. Graybill, and D. C. Boes, *Introduction to the Theory of Statistics* (McGraw Hill, 1974), 3rd ed.

[43] B. T. Cleveland, Nucl. Instrum. Methods Phys. Res., Sect. A **214**, 451 (1983).